Microelectronic Engineering 301 (2026) 112397

Contents lists available at ScienceDirect

Microelectronic Engineering

journal homepage: www.elsevier.com/locate/mee

Research paper

Digital filter on FPGA for subcellular resolution electrophysiology using a high-density CMOS-based microelectrode array☆

Maximilian Ell, Ahmet Büyükakyüz, Paul Werginz, Günther Zeck *

Institute of Biomedical Electronics, Faculty of Electrical Engineering and Information Technology, TU Wien, Vienna, Austria

ARTICLE INFO

Keywords:
CMOS microelectrode array
Adhesion noise spectroscopy
Real-time systems
Field programmable gate array
Digital signal processing
Ex vivo retina
Electrophysiology

ABSTRACT

CMOS-based microelectrode arrays (MEAs) are used to record the electrical activity in neural tissues down to micron-scale cellular structures at high spatiotemporal resolution. Continuous recording of extracellular voltages would, however generate large datasets with very sparse spatial and temporal information. Towards an efficient strategy, we propose here a Field Programmable Gate Array (FPGA) which filters the continuous CMOS MEA data stream sampled at 28 kHz and extracts electrophysiological relevant information.

In a first step, sensors of interest are selected based on the electrical label-free identification of those sensors covered by the neural tissue via adhesion noise spectroscopy. The adhesion noise-based electrical imaging is validated against light microscopic images. The FPGA finite impulse response (FIR)-filtered data is validated against software-based post-processed data.

In a second step, we implement a spike-triggered average (STA) algorithm to identify and visualize electrical activity at subcellular resolution in retinal neurons, which allows for the tracking of axonal signal propagation within the neural tissue.

This label-free, non-invasive method enables the localization of sensors of interest for electrophysiological recordings and the extraction of neuronal signals. It represents a significant advancement in neuroscience tools, which facilitates the study of neuronal network dynamics at unprecedented spatiotemporal resolution.

1. Introduction

The neuronal signaling pathway conveys information from the site of initiation to synaptically connected cells within neuronal networks using electrical signals (e.g., action potentials, APs). Monitoring neuronal activity, reflected by small voltage deflections, provides insights into the communication within these neuronal networks. Understanding the mechanisms and features of these networks requires methods that enable the interaction with neuronal functional subunits and ensembles – somas, axons, dendrites, single neurons, as well as entire networks – at high spatiotemporal resolution and in real-time [1–3].

Commercially available standard microelectrode arrays (MEAs) constitute an established technology to record from single neurons and networks thereof [4–6]. However, passive MEAs suffer from their low spatial resolution (electrode pitch >30 μm) and constrained number of electrodes (<300), and therefore neither allow for recording morphological details of individual neurons nor for monitoring large neural networks [7,8].

Progress in complementary metal-oxide-semiconductor (CMOS) technology also enabled the translation of MEAs into biotechnology. CMOS MEAs comprise thousands of densely packed recording sites and are used to study biological network activity at high spatial (<10 μm, thus smaller than cell body size) and high temporal resolution (~20 kHz bandwidth) [8,9]. Hence, CMOS MEAs have been used to record spontaneously occurring axonal signals in the retina [10,11] and axonal and potentially dendritic signals in elaborate neurites of dissociated neurons [12]. These high-density MEA arrangements enable us to record the electrophysiological activity of neuronal tissue with subcellular resolution, which presents a key technical challenge in neuroscience to sample fine-scale structures [13].

However, the recorded extracellular voltage signals are impaired by biological and electronic noise sources, which makes it impossible to detect neuronal APs (spikes) without filtering the raw data. The online

☆ This article is part of a Special issue entitled: 'AMNDCE' published in Microelectronic Engineering.

* Corresponding author at: Gusshausstrasse 27-29, 1040 Vienna, Austria.
E-mail addresses: maximilian.ell@tuwien.ac.at (M. Ell), ahmet.bueyuekakyuez@tuwien.ac.at (A. Büyükakyüz), paul.werginz@tuwien.ac.at (P. Werginz), guenther.zeck@tuwien.ac.at (G. Zeck).

https://doi.org/10.1016/j.mee.2025.112397
Received 30 January 2025; Received in revised form 24 July 2025; Accepted 18 August 2025
Available online 20 August 2025
0167-9317/© 2025 The Authors. Published by Elsevier B.V. This is an open access article under the CC BY license (http://creativecommons.org/licenses/by/4.0/).

processing of a data stream of numerous sensors (>10 k) at high sampling frequency demands powerful computational performance, which is not easily achievable on a standard computer architecture. Therefore, we propose here a CMOS MEA data streaming setup that extracts the neuronal activity of an active neural tissue by filtering the recorded signal with a field programmable gate array (FPGA), meeting real-time requirements. Since a full readout of all sensor sites is currently not feasible at a sampling frequency of 20 kHz, we electrically determine the sensors of interest covered by the retina tissue [14] using adhesion noise spectroscopy [15]. The electrical identification of the retina tissue allows for the recording of sparsely distributed regions on the CMOS MEA, where retina patches with densely packed ganglion cells require high-density arrangements. We localize single retina neurons in terms of spatiotemporal maps to track the neuronal signal with subcellular resolution. The most common method to electrically image signal propagation is based on spike-triggered average (STA) algorithms. The STA is computed by extracting and aligning multiple AP snippets of the extracellular recording. Next, averaging the spike traces reduces the noise and visualizes the AP [16].

The electrical image of retina tissue based on the adhesion noise map is compared with ground truth light microscopic images, and the FPGA-filtered data of the electrophysiological recording is compared with software-filtered post-processed data. The technology presented in this work provides a label-free, non-invasive, and fast tool to locate sensors of interest for neural tissue recordings and filtering data via FPGA to extract electrophysiological relevant information suited for real-time applications.

2. Methods

2.1. Electrical recording with CMOS microelectrode arrays

The CMOS microelectrode array (MEA) system CAN-Q Station with the biosensing platform CAN-Q Chip (obtained from formerly Venneos GmbH) features 256 × 384 capacitive recording sites with a sensor pitch of 5.6 µm × 6.5 µm covering an active area of 1.6 mm × 2.5 mm as described in [17,18]. The sensor array was covered with an inert 30 nm ALD-TiO_2 top oxide layer to enable the capacitive coupling of a biological sample with the underlying field-effect transistor [14]. A Perspex culture chamber was glued on the chip, which insulated the bond contacts and exposed the recording sites to the retina and medium [19]. We employed an external Ag/AgCl electrode (VWR International GmbH) as a reference electrode to calibrate the MEA using the CAN-Q Acquisition software (Venneos GmbH) with default settings.

2.2. Extracellular electrophysiology of the ex vivo retina

We recorded extracellular voltages from the ex vivo retina of adult mice using the CMOS MEA. The dissection of the retina was conducted following previously established protocols [16,20]. Before placing the retina, we cleaned the MEA with Tickopur R60 (5 % *v*/v at 80 °C, Dr. H. Stamm GmbH Chemische Fabrik), sterilized it with 70 % v/v ethanol and UV light for 30 min, and rinsed it with distilled water. The MEA's recording sites were coated with 0.01 µg/µL Poly-L-lysine (PLL) (50 µL, MW 150–300 kDa, Sigma-Aldrich GmbH) for 2 h at room temperature to ensure tight tissue adhesion. Afterwards, we washed the MEA with PBS (1×) to remove the excessive coating solution. Next, a portion of the isolated retina (ca. 3–4 mm^2) was placed on the MEA, which we gently pressed with a membrane for a few seconds to flatten it completely. The chip's chamber containing the retina sample was filled with appropriate electrolyte to guarantee cell viability. We assessed the spectral power density (S_V) of the extracellular voltage at 300 kHz to probe the retina-chip interface for sufficient electrical recording capability. Next, we recorded neural activity with the CMOS MEA at a 28 kHz sampling rate. The MEA and recording hardware were placed in a safety cabinet at room temperature without additional shielding during the recordings.

2.3. Datastream setup

The CMOS MEA system (CAN-Q Station) is the central hub (s. Fig. 1A top) and is equipped with on-board ADCs (Supplementary Fig. S1), which amplify and digitize the extracellular voltage signals at a resolution of 14 bits and a total sampling rate of 14.4 MHz [21]. The recorded data are streamed from the CAN-Q Station to the host-PC with a remote procedure call (RPC) server connected via an Ethernet hub.

2.4. Field programmable gate array (FPGA) filter

Filtering reduces the total noise amount and removes the offset and the local field potential (LFP) components, which are low-frequency extracellular voltages generated by the summed electric current flowing from multiple nearby neurons [22,23]. The recorded raw extracellular voltages were high-pass-filtered with a finite impulse response (FIR) filter with a cutoff frequency of 400 Hz. Therefore, we designed the filter on an FPGA using Vivado Design Suite (version 2018.2, provided by AMD / Xilinx) for the hardware integration (s. Fig. 1B top). We operated with the PYNQ-Z1 Board (Digilent) as the development kit, which is compatible with the ZYNQ MP ZU4EG Board of the data stream hub architecture. We designed the filter using the FIR Compiler IP core from the Vivado Design Suite. The high-pass filter coefficients (taps) were extracted from MATLAB's extension Filter Design HDL Coder. We then imported the taps into the IP core to build the FIR Compiler. Next, we configured the AXI Stream interface and the remaining parameters with the Vivado GUI. We selected the systolic multiply-accumulate architecture with a pipelined direct-form structure, which is optimized for digital signal processor (DSP) slice utilization with area-efficient and high-performance implementation as described in [24–26]. Furthermore, the direct-form structure saves resources by exploiting coefficient symmetry. Finally, we implemented the configured IP core on the FPGA's programmable logic (PL) (i.e., PYNQ-Z1 Board) [27].

We used the Advanced eXtensible Interface (AXI)-Stream Protocol as the on-chip communication system between the FPGA components, which is optimized for large data real-time processing (Fig. 2B). The AXI direct memory access (DMA) engine provides high-performance memory access between the system memory and AXI4-Stream type target hardware components, allowing the central processing unit (CPU) (i.e., host-PC) to offload data transfer control and filtering execution to hardware automation [28]. We designed the FIR Compiler using Vivado's IP Core FIR filter block design (s. Fig. 2C and D). The high-pass filter coefficients (taps) were generated using the MATLAB (version 24.1.0.2603908 (R2024a) Update 3) extension Filter Design HDL Coder (version 24.1 (R2024a)). Next, we configured the FIR Compiler with the estimated taps in Vivado (s. Fig. 2C). Afterwards, Vivado's behavioral simulation confirmed the logical integrity of the filter design's syntax, functionality, and various connections. We converted the VHDL design into logic gates via Synthesis to optimize the timing constraints of the circuit components. The Implementation then mapped the synthesized design to the FPGA's resources [29]. Finally, we generated a bitstream to configure the hardware logic, routing, and initial values on the PYNQ-Z1 Board, enabling the FPGA-based FIR filtering of the retina sample data (s. Fig. 1C).

2.5. Filter setup

For the FIR filter setup, we determined the filter coefficients using the MATLAB Filter Design HDL Coder to 198 as the minimum order for a proper magnitude response and minor oscillations at a cutoff frequency of 400 Hz (s. Fig. 1B) [30]. With this configuration, the hardware uses 8446 LUTs, 2 BRAMs, and 100 DSP slices with a power consumption of 1.54 W, as reported by Vivado.

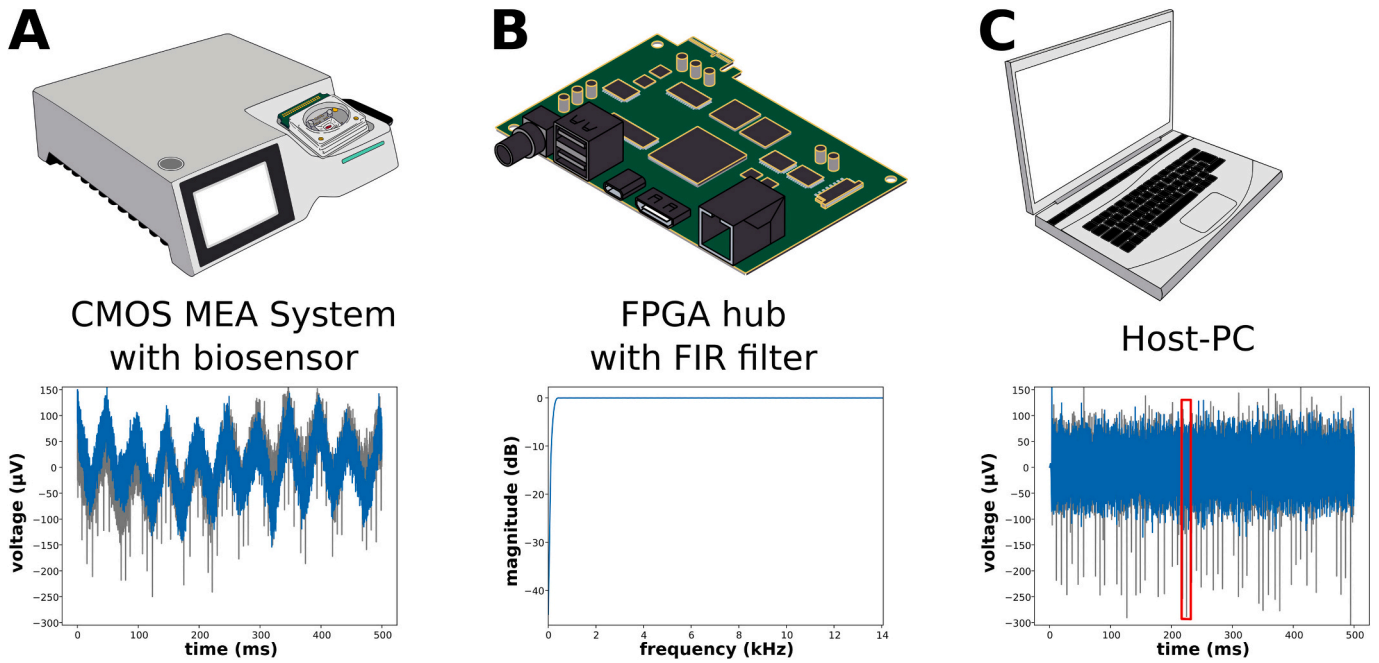

Fig. 1. Data stream processing of real-time filter setup. (A) Top: Data acquisition from a biological sample using a CMOS microelectrode array (MEA) biosensing platform. Bottom: Raw extracellular voltage traces of selected sensor sites on the MEA (blue: voltage trace from bare sensor site, grey: voltage trace from a sensor with retina attached). (B) Top: Field programmable gate array (FPGA) board used for data filtering with a finite impulse response (FIR) filter. Bottom: Magnitude response of designed FIR filter. (C) Top: Host-PC as central processing unit. Bottom: FPGA-FIR-filtered data of selected sensor sites (blue: FIR-filtered voltage trace from bare sensor site, grey: FIR-filtered voltage trace from a sensor with retina attached with action potentials, exemplary marked red). (For interpretation of the references to colour in this figure legend, the reader is referred to the web version of this article.)

2.6. Filter validation

To validate the FIR filter against ground truth, the raw data was FIR-filtered via FPGA and high-pass filtered using a 4th-order Butterworth filter via Python (version 3.9.5). We analyzed the two signals (i.e., hardware- and software-filtered) on inconsistencies.

2.7. CMOS MEA voltage noise analysis

We analyzed the spectral power density S_V like an electrical image with image processing techniques using the OpenCV Library via custom Python scripts [15]. Firstly, we subtracted the S_V of the bare electrodes (i.e., background noise) from the retina recordings to extract the adhesion noise, assuming uncorrelated noise sources [14]. Secondly, a Gaussian Blur filter reduced the amount of image noise via grey-scaling and blurring, which enhanced the identification of objects of interest (i.e., the retina) [31]. Thirdly, we determined the segmentation threshold using Otsu's Binarization method [32]. Lastly, morphological operations (i.e., opening, closing) fine-tuned the object detection and recognition.

To recover axon positions of the retina tissue, we performed spike-triggered averaging (STA) of the FIR-filtered extracellular voltage traces. The STA algorithm computes the mean voltage signal of a spike across the MEA by aligning multiple spikes of a single neuron to their timing and averaging the resulting waveforms. The result yields a voltage trace with reduced noise, enabling the detection and tracking of the axonal signal [10,33] and to obtain electrical images of one single ganglion cell neuron in terms of spatiotemporal maps [34]. Spike detection was performed by FIR-filtered voltage trace thresholding.

2.8. Microscopy validation of electrical imaging

We related the brightfield images, taken with an upright light microscope (Zeiss Axioplan, ×10 objective, Carl Zeiss AG), to the electrically estimated tissue position to ground truth. For the CMOS MEA imaging, we stitched together the whole microscopic image from individual image parts with the Fiji (Fiji is just ImageJ, version 1.54f) plugin Stitching described in [35]. For the brightfield microscopy imaging, we segmented the retina tissue via Photos' (version: 2024.11100.16009.0, Microsoft) Background Remove Editor.

3. Results

The presented work designed a filter on a field programmable gate array (FPGA) for real-time analysis of the electrophysiological activity of retina tissue. The implemented capabilities of the FPGA finite impulse response (FIR) filter were tested and experimentally characterized by processing the signal from an ex vivo retina sample. The CMOS microelectrode array (MEA) in operation with the FPGA FIR filter enabled simultaneous spike recordings of the same neuron from different sensor sites with high temporal resolution and the electrical imaging of single neurons in terms of spatiotemporal maps.

For the retina experiment, we first electrically identified the sensors (i.e., electrolyte-oxide-silicon field-effect transistors) of interest on the CMOS MEA, which are in contact with the retina (Fig. 3A, red contours). The electrical detection of biological samples on the CMOS MEA via adhesion voltage noise spectroscopy is described in [15]. In brief, we recorded the voltage generated in the cleft between the retina tissue and a sensor's oxide surface and estimated the spectral power density (S_V) of the voltage fluctuations. The resistive cleft below the retina gives rise to the adhesion voltage noise, which allows us to distinguish this value from that of a bare sensor site (s. Fig. 3Ci) [14], [36,37]. The adherent retina was detected by evaluating the S_V spectrum. We assessed the S_V spectrum of the voltage noise from three different positions on the chip, i.e., i) adhesion area of the retina (Fig. 3A Δ), ii) sensor under the retina with poor attachment (Fig. 3A ◊), and iii) bare, uncovered sensor (Fig. 3A ✶). Fig. 3Ci demonstrates that the retina adhered to recording sites increased the S_V across the entire frequency spectrum (Δ, red trace), which is attributed to the resistive cleft [14,38]. For the retina segmentation, we selected a frequency value in the middle of this frequency range, i.e., 300 kHz, and extracted the contours (Fig. 3A, red

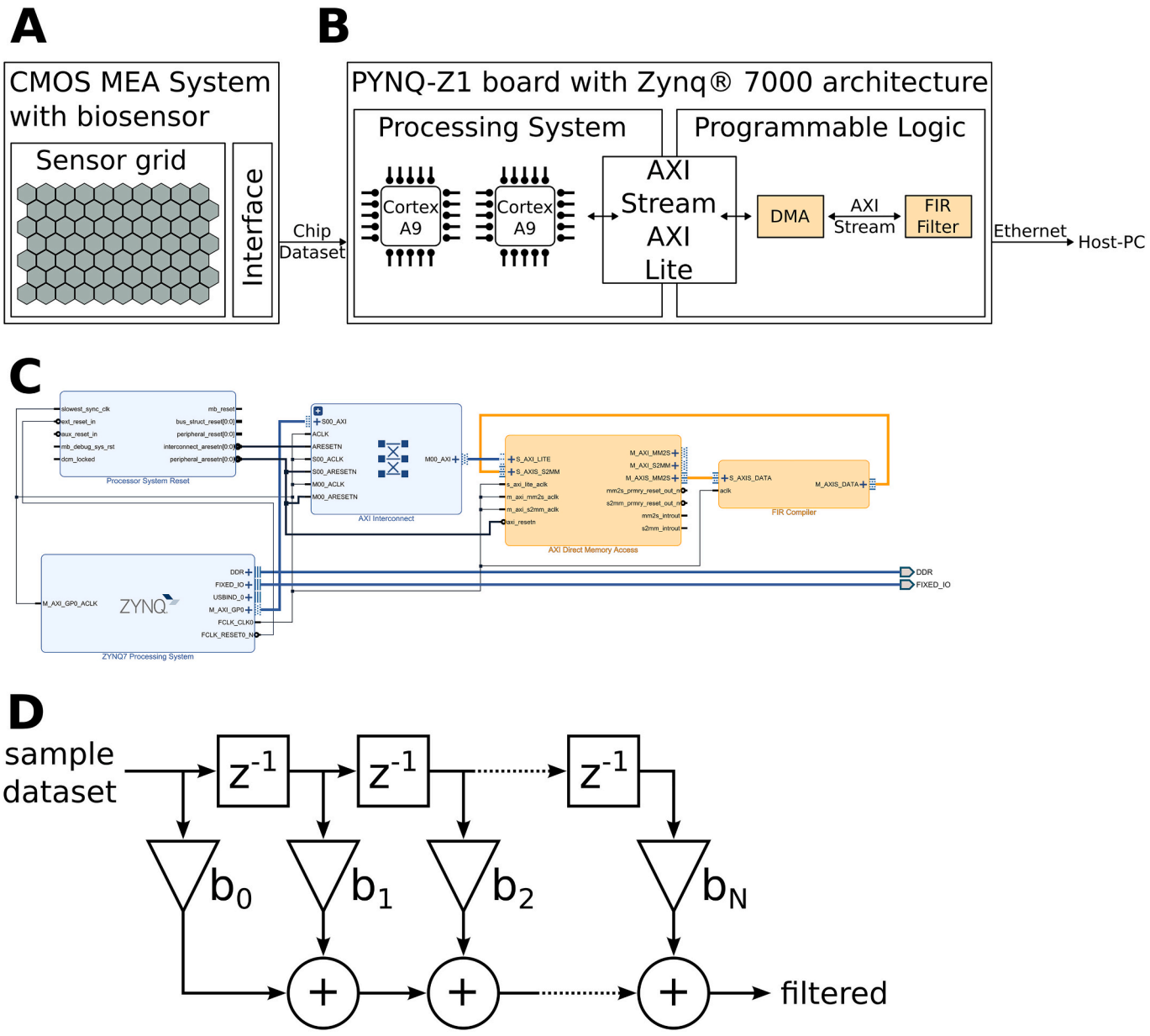

Fig. 2. Configuration scheme of finite impulse response (FIR) filter periphery. (A) Data acquisition via CMOS microelectrode (MEA) system with biosensing platform. (B) Field programmable gate array (FPGA) Zynq-7020 SoC architecture. The processing system (PS) works with two Cortex A9 processors, and the finite impulse response (FIR) filter (highlighted in orange) is configured in the programmable logic (PL) part. Direct memory access (DMA) provides high-performance memory access between the system memory and the FIR filter. On-chip communication between the FPGA components PS and PL is enabled via advanced eXtensible interface (AXI)-Stream Protocol. The first in first out (FIFO) handles data buffering applications. (C) Vivado block design of FIR filter periphery. Highlighted in orange: IP Core FIR filter block design with AXI direct memory access (DMA) interface and FIR Compiler. (D) Direct form discrete-time FIR filter of order N. z^{-1} units work as delay operators, b_0-b_N are the filter coefficients (i.e., taps).

contours) as described in the method section (following [15]). Fig. 3Ci also illustrates that the S_V spectrum of sensors under the retina at position ◊ (Fig. 3A) aligned with the S_V spectrum of bare sensors (Fig. 3A ∗), which showed poor attachment and therefore no significant contribution of the cleft to the voltage noise. We found 85 % accuracy in the estimated retina position from the voltage noise S_V and brightfield microscopy via overlay (Fig. 3A and B).

Next, we recorded the extracellular voltage at the three indicated sensor positions on the CMOS MEA in Fig. 3A, i.e., Fig. 3Cii at position Δ, Fig. 3Ciii at position ◊, and Fig. 3Civ at position ∗, and high-pass-filtered the data with the FPGA FIR filter, meeting real-time requirements. The voltage trace in Fig. 3Cii revealed an active retina in the electrically identified adhesion area detected by action potentials that cross the spike threshold. We calculated the retina's firing rate (FR) to 122 Hz over 500 ms, indicating a highly active retina tissue [39]. The sensor under the retina in the area of poor tissue attachment (position ◊) did not record spikes but voltage noise only (Fig. 3Ciii) and aligned with the voltage recording of a bare sensor (Fig. 3Civ, position ∗).

After successful electrical detection of the retina on the CMOS MEA via adhesion voltage noise spectroscopy, we analyzed the retina spikes from side-by-side sensors to demonstrate our biosensing system's capability to simultaneously record spikes of the same neuron from neighboring sensors with high spatiotemporal resolution. This allows us to detect different signals on different sensors of many cells and subcellular structures. The FIR and digital filters were compared in terms of signal-to-noise ratio (SNR).

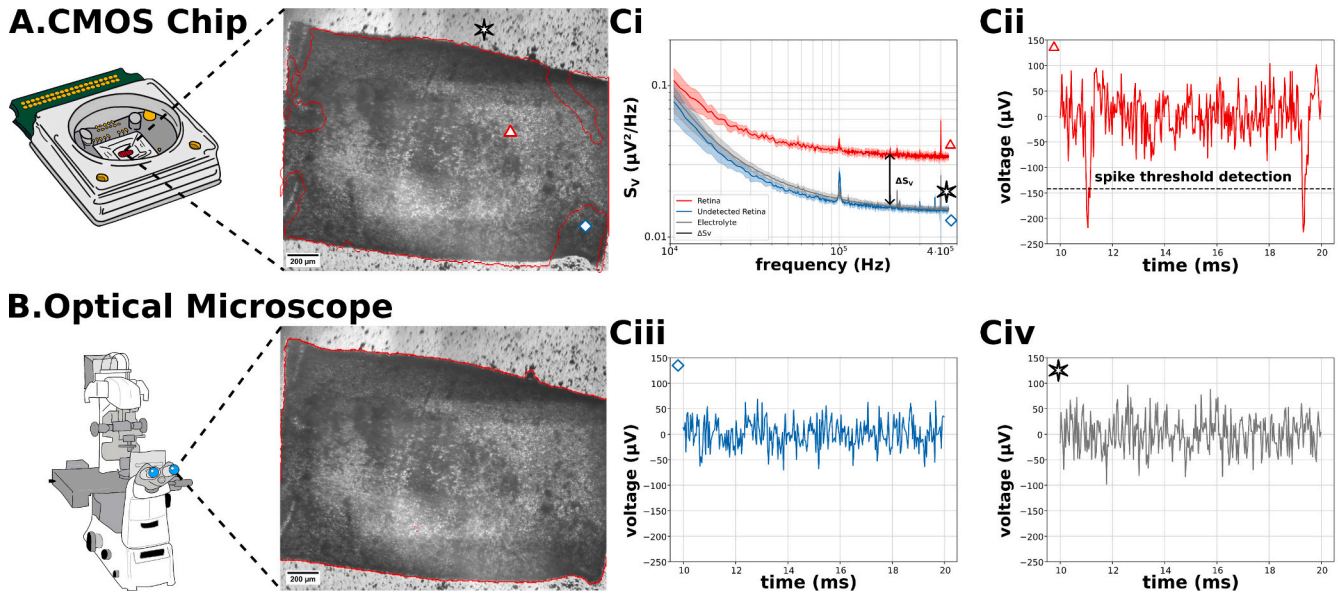

Fig. 3. Experimental workflow of electrical retina detection with spectral power density (S_V, evaluated at 300 kHz) and sensor selection with field programmable gate array (FPGA) finite impulse response (FIR) filter-extracted action potentials. (A) Overlay of electrical imaging of retina tissue on the CMOS microelectrode array (MEA) (red contours via S_V-analysis at 300 kHz) with brightfield microscopy imaging (dark grey/black: retina sample, light grey: sensor sites as background). The symbols (Δ, ◊, and ∗) indicate different sensor positions on the CMOS MEA, i.e., Δ: sensor with attached and electrically identified retina, ◊: sensor under electrically undetected retina, and ∗: bare sensor from area without retina. (B) Brightfield microscopy image with Photos-based retina segmentation (red contours). (Ci) Electrical retina detection via adhesion voltage noise spectroscopy [15]. A retina-covered sensor (Δ, red trace) exceeded the sum of ΔS_V and the values of S_V of bare sensors (i.e., ∗, grey trace). The S_V of a sensor under the retina with poor tissue attachment aligned with the S_V of bare sensors (◊, blue trace). (Cii) FIR-filtered voltage trace of retina-covered and -detected sensor at position Δ in (A) with spikes exceeding the spike threshold of 140 µV. (Ciii) Recorded voltage without spikes after FIR filtering of a sensor under the retina tissue at position ◊ in (A), which was not electrically identified via adhesion voltage noise spectroscopy. (Civ) FIR-filtered voltage trace of an uncovered, bare sensor at position ∗ in (A). (For interpretation of the references to colour in this figure legend, the reader is referred to the web version of this article.)

We studied the voltage traces of neighboring sensors after FIR and digital filtering (Fig. 4). The insets A and B indicate the sensor positions on the CMOS MEA sensor grid (Fig. 4, top) and the corresponding FIR- and digital-filtered voltage recordings. Two features could be extracted from the recordings: i) the recorded spikes maintained the same shape for both filter types (Fig. 4A Overlay), but ii) the spikes exhibited higher amplitudes for the FIR filter (−233 µV, Fig. 4A top and 4B top) than for the digital filter (−138 µV, Fig. 4A and B center). We determined the SNR for the FIR filter to be 13.2 dB and for the digital filter to be 12.7 dB (Fig. 4C, statistically significant with $p < 0.05$). Filtering increased the SNR for both filter types, i.e. by 1.1 dB for the FIR filter and by 5.2 dB for the digital filter (s. Supplementary Fig. S2).

Based on the FPGA FIR and digital filter comparison (Fig. 4A), we confirmed that the FPGA FIR filter operated correctly by maintaining the same spike patterns for FIR- and digital-filtered voltage traces of neighboring sensors. Next, we recovered neuron positions from spike-triggered averaging (STA) of the extracellular voltages by electrical images in terms of spatiotemporal maps [10,33,34].

We generated an electrical image from the STA's standard deviation to locate a single retina neuron on the CMOS MEA (Fig. 5A). The location of the soma is determined on or next to the sensor. The STA's standard deviation enabled us to identify a sensor with i) highly active spiking activity (i.e., high standard deviation, Fig. 5A-1), ii) moderately active spiking activity (i.e., moderate standard deviation, Fig. 5A-2), iii) attenuated spiking activity (i.e., low standard deviation, Fig. 5A-3), and iv) a sensor without recorded spikes (i.e., lowest standard deviation, Fig. 5A-4) (note: sensor position 3 and position 4 are equally distant from position 1). In Fig. 5B, we inferred the average voltage traces corresponding to the sensor positions on the CMOS MEA. At position 1, we recorded the STA with the highest amplitude (−237 µV) (Fig. 5B-1). At position 2, the STA's amplitude decreased to −105 µV (Fig. 5B-2) and further attenuated to −19 µV at position 3 (Fig. 5B-3). The STA of the sensor at position 4 revealed no spike activity (Fig. 5B-4).

As the action potentials propagate along the axon and the neuron cell network of the retina, we recorded spikes of different patterns. The STA then allows for tracking the spike across the CMOS MEA. We normalized the FIR-filtered voltage traces from positions 1 and 3 (Fig. 5C). Sensor 3 recorded the spike 0.14 ms earlier than sensor 1, indicating the signal propagation from sensor 3 to 1 (as highlighted in Fig. 5A). With a sensor distance of 70 µm, we determined the action potential propagation speed to 0.5 m/s. The action potential propagation velocity is lower than in the literature [11,40,41] since we recorded at room temperature and not between 35 and 37 °C [10].

4. Discussion

In this study, we demonstrated a high-density CMOS microelectrode array (MEA) with the data stream finite impulse response (FIR) filter on a field programmable gate array (FPGA) for the electrophysiological recording of retina tissue. The electrical detection of the retina via adhesion noise spectroscopy enabled us to select the sensors of interest (i.e., retina-covered sensors), yielding high-quality recordings of neuronal action potentials. Optical microscopy validated the electrical retina detection. With the high spatiotemporal resolution, the CMOS MEA system allowed for single-cell studies at subcellular resolution and spike recordings of different patterns from different sensor sites with high temporal resolution.

After placing the retina on the CMOS MEA, optical microscopy failed to identify the sensor sites with tight retina tissue attachment, which is needed for the electrophysiological voltage recordings (Fig. 3B). Hence, the electrical retina detection using the spectral power density (S_V) of the voltage fluctuations proposes an accurate way to determine the sensors of interest (i.e., retina-covered and -detecting sensors) (Fig. 3A and Cii). Recording sites with tight retina attachment exhibit a higher S_V

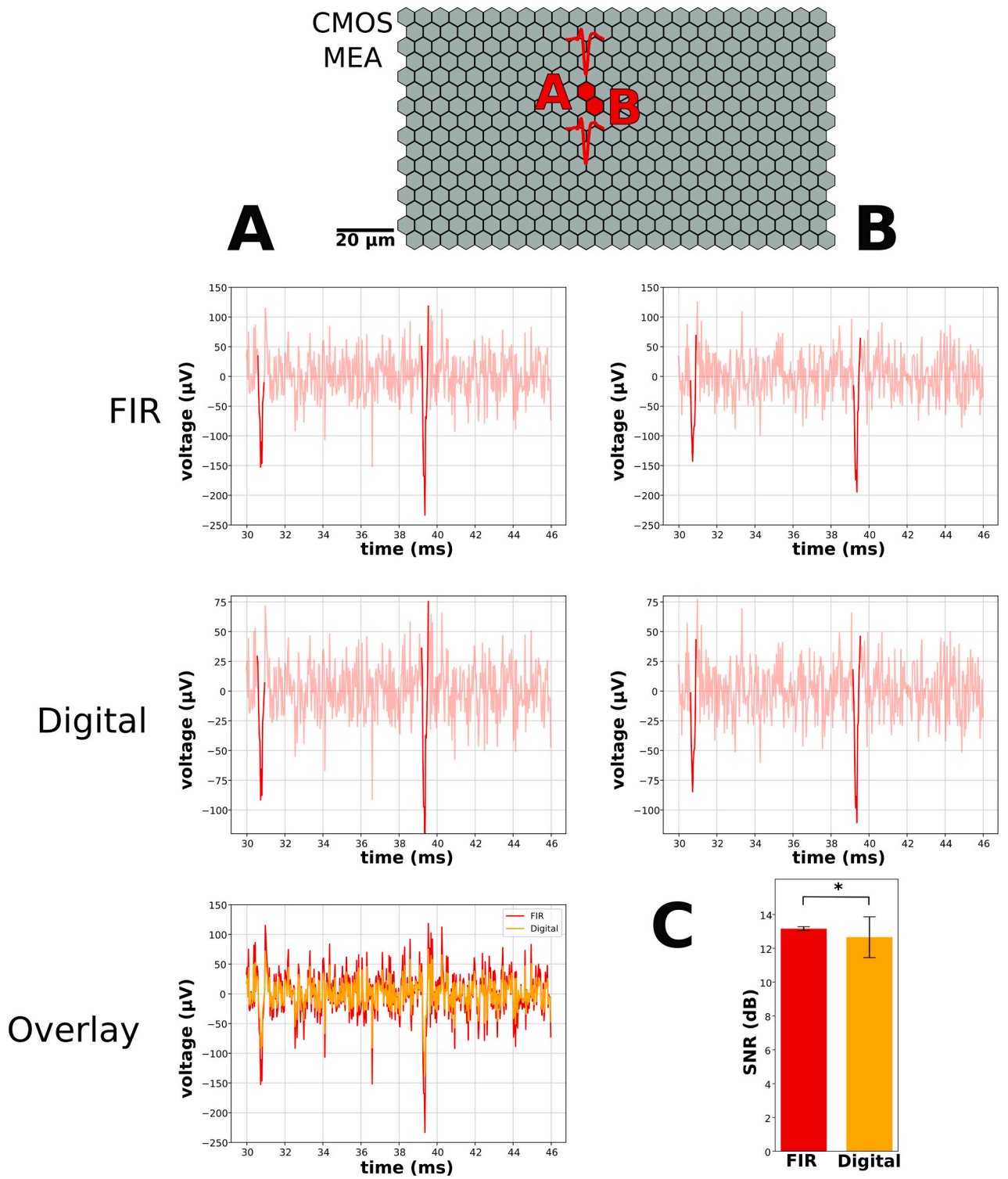

Fig. 4. Finite impulse response (FIR) and digital-filtered voltage traces of simultaneously recorded spikes from different neighboring sensors compared in terms of signal-to-noise ratio (SNR). (A) Voltage recordings of sensors side-by-side demonstrated the CMOS microelectrode array (MEA)'s simultaneous recording capability of the same signal from different sensors. FIR and digital-filtered voltage recordings of position A in the CMOS MEA sensor grid (top) showed spikes at the same time but with different amplitudes. The FIR-filtered voltage recording exhibited spike amplitudes from −146 µV to −233 µV and digital-filtered spikes from −92 µV to −138 µV (Overlay: FIR-filtered data (red trace), digital-filtered data (orange trace). (B) Recorded voltage traces of sensor position B in the CMOS MEA sensor grid. FIR-filtered spike amplitudes ranged from −143 µV to −194 µV, and digital-filtered amplitudes were between −85 µV and − 111 µV. (C) The signal-to-noise ratio (SNR) of the FIR filter was 13.2 dB, and of the digital filter 12.7 dB; error bars indicate the standard deviation (FIR filter: 0.12 dB, digital filter: 1.2 dB. Asterisks: ns, not significant. *, $p \leq 0.05$). (For interpretation of the references to colour in this figure legend, the reader is referred to the web version of this article.)

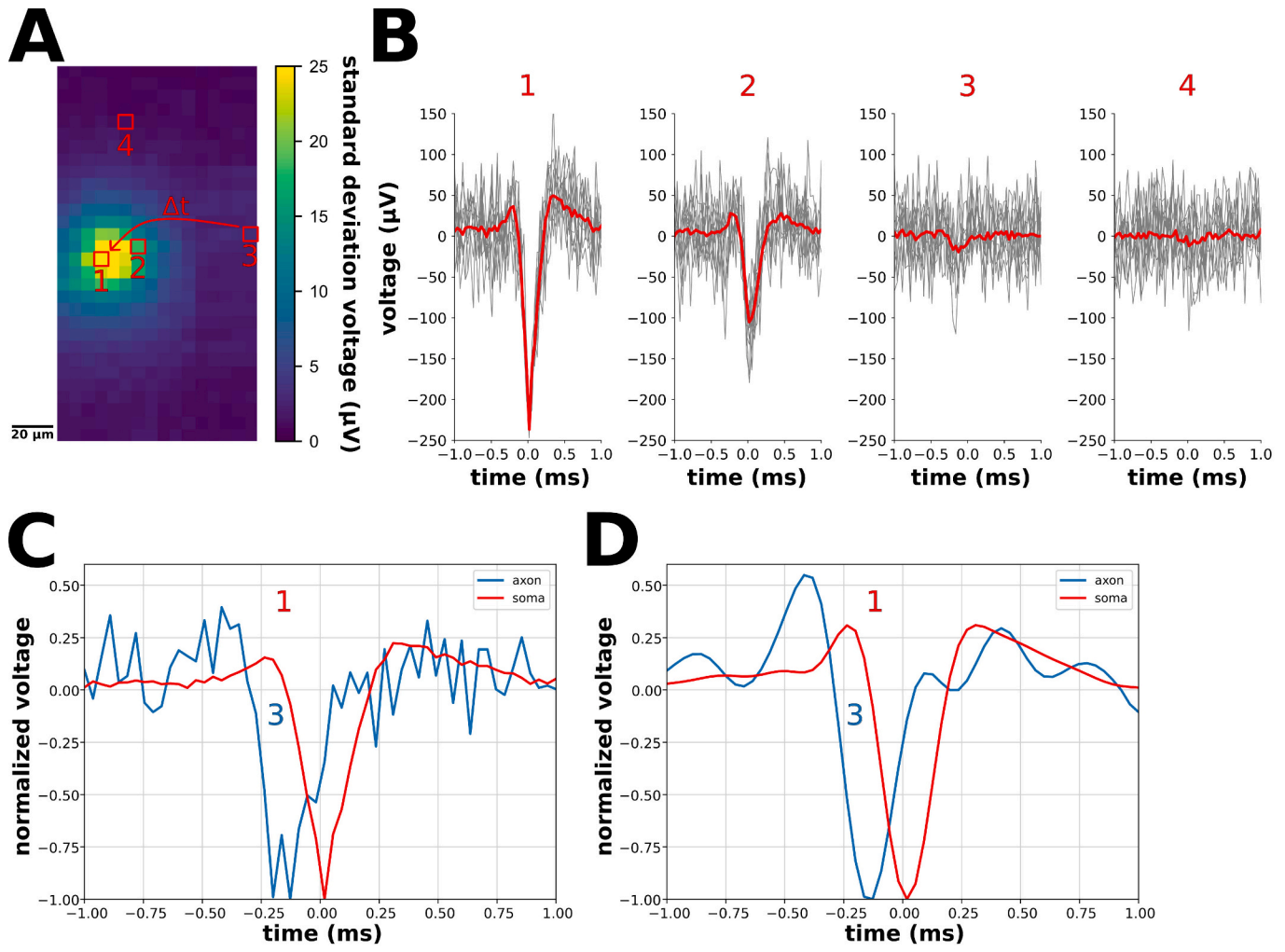

Fig. 5. Electrical imaging and spike analysis of one neuron in the retina obtained by spike-triggered average (STA) of voltage recordings. (A) Electrical image of one single neuron in terms of a spatiotemporal map, shown as a heat map of the standard deviation of the STA. A high standard deviation (i.e., green-yellow area) of the STA indicates the region of the firing neuron. A low STA's standard deviation is areas with low or no neural activity. (B) Numbered voltage waveforms (i.e., 1–4) inferred from the CMOS MEA positions in (A). We calculated the mean voltage signal of a spike (red trace) by averaging multiple spikes of a single neuron (grey traces) aligned by the spike timing [10]. Sensor positions 3 and 4 are equally distant from position 1; the sensor at position 3 recorded an attenuated action potential, and the sensor at position 4 recorded voltage noise. (C) Normalized FIR-filtered voltage trace of sensor at positions 1 and 3 revealed signal propagation from 3 to 1 in 0.14 ms. (D) Normalized bandpass-filtered voltage traces of the same sensors as in (C). (For interpretation of the references to colour in this figure legend, the reader is referred to the web version of this article.)

amplitude than sensors with poor attachment or bare sensors over the whole frequency range (Fig. 3Ci), which is in accordance with prior studies on the neuron-transistor interface [14,19,38]. From a methodological perspective, future work could avoid retina protrusions while placing the tissue on the chip or enable a retina flattening workflow to enhance the tissue attachment to the CMOS MEA's surface. Moreover, an algorithm could enable an automated sensor selection for the voltage recording of electrically detected retina tissue.

The sensors with the electrically identified retina demonstrated spike recording capabilities with high temporal resolution (Fig. 3Cii), sufficiently high for reliable spike identification. In the future, to fine-tune the automated sensor selection for the electrophysiological recordings, the FPGA FIR filter could implement a threshold spike detector after filtering while meeting real-time requirements. Moreover, to handle more channels at once, we (i) add extra one-dimensional filter chains, or (ii) group channels into a small 2-D systolic grid, by keeping the same multiply accumulate (MAC) structure for both options [24–26].

The CMOS MEA offers both the capability to record spikes simultaneously from neighboring sensors (Fig. 4A) and spikes from distant sensors with various patterns (Fig. 5B). To validate the data filter process, we compared the FIR and digital filter in terms of signal-to-noise ratio (SNR). Both filters revealed the same spike patterns, but the FIR filter provided a higher SNR (Fig. 4C). This is due to the high number of used taps (i.e., 198 [30]) for the FIR filter. However, a 4th-order Butterworth filter (i.e., the digital filter) performs better for real-time applications [42,43]. Therefore, we must consider the tradeoff between SNR and speed performance for future applications to meet real-time requirements.

The high spatial resolution of the CMOS MEA localized a single retina neuron from spike-triggered averaging (STA) of the extracellular voltages in terms of spatiotemporal maps (Fig. 5A) [10,33,34]. Moreover, we recovered the soma and axon by tracking the action potential propagation over multiple electrodes (Fig. 5B1-3), while equally distant sensor sites revealed no electrophysiological activity (Fig. 5B-4). The resulting electrical image from spatiotemporal maps holds the potential to track the axonal signal with subcellular resolution, which may provide new insights into the initiation of action potentials [34,44] and signaling pathways within neural networks [45,46]. We inferred from

the STA that the signal propagated from the axon to the soma with a velocity of 0.5 m/s (Fig. 5C). Although the bandpass-filtered signal (Fig. 5D) revealed a more accurate spike pattern than the FIR-filtered one (Fig. 5C), the presented FIR filter on FPGA is designed for the real-time analysis of the neuronal signals and qualitatively matches the post-recording analyses.

The presented CMOS MEA system offers one of the smallest electrode pitches (~6 μm) among published systems and therefore provides one of the highest spatial resolutions reported in literature for extracellular neural signal detection [8–13]. State-of-the-art recording systems allow for recording at spatial resolution ranging between 6 and 17.5 μm. Some systems provide full readout of all sensors at the cost of increased noise level (rms of few tens of μV) [10,11,14], while others systems are optimized for low-noise recording (rms of few μV) at the cost of a reduced number of simultaneously recorded channels [8,13]. Note, that CMOS technology enables the detection of particles at even smaller resolution (~1 μm) using capacitive sensors, which operate in the MHz range [47–49] are beyond the scope of this study. Adhesion noise spectroscopy electrically images only the parts of the retina that are tightly attached to the CMOS MEA's sensors and therefore suited for electrophysiological recordings, while brightfield microscopy images the whole tissue on the chip, adhered and or not.

5. Conclusion

We successfully developed and implemented an FPGA-based finite impulse response (FIR) filter into our CMOS microelectrode array (MEA) setup to extract electrophysiological relevant information from retina tissue. The key innovation of this work is the neural signal processing pipeline, which identifies the sensors of interest (i.e., sensors with the attached retina) on a high-density CMOS MEA using adhesion noise spectroscopy and filters the dataset via an FIR filter on an FPGA to reveal action potentials (APs), meeting real-time requirements. The noise-based imaging proved superior to optical microscopy for selecting electrophysiological active recording sites, as it also unveiled sensors below the retina tissue with poor tissue attachment, which are not suitable for AP recording and which were optically not visible (Fig. 3Ciii). The selected sensors yielded high-quality neuronal action potentials (Fig. 3Cii).

To achieve a fully automated neural signaling pipeline for high-quality electrophysiological recording, future work will focus on (i) refining the automated sensor selection process [34], (ii) incorporating threshold spike detection via FPGA for real-time AP analysis, and (iii) exploring detailed physiology [46] using the high spatial resolution of the CMOS MEA.

CRediT authorship contribution statement

Maximilian Ell: Conceptualization, Methodology, Software, Validation, Formal analysis, Investigation, Data curation, Writing – original draft, Writing – review & editing, Visualization. **Ahmet Büyükakyüz:** Methodology, Software, Formal analysis, Investigation, Writing – review & editing. **Paul Werginz:** Methodology, Software, Validation, Data curation, Visualization. **Günther Zeck:** Conceptualization, Validation, Resources, Writing – original draft, Writing – review & editing, Supervision, Project administration, Funding acquisition.

Declaration of competing interest

The authors declare that they have no known competing financial interests or personal relationships that could have appeared to influence the work reported in this paper.

Acknowledgment

We thank Dr. Ralf Zeitler for the development of the RPC server and Dr. Andrea Corna for the retina preparation. This work was supported by the Austrian Science Fund (FWF) under Grant 10.55776/P35488.

Appendix A. Supplementary data

Supplementary data to this article can be found online at https://doi.org/10.1016/j.mee.2025.112397.

Data availability

Data will be made available on request.

References

[1] A.P. Alivisatos, et al., Nanotools for neuroscience and brain activity mapping, ACS Nano 7 (3) (Mar. 2013) 1850–1866, https://doi.org/10.1021/nn4012847.
[2] G. Buzsáki, et al., Tools for probing local circuits: high-density silicon probes combined with optogenetics, Neuron 86 (1) (Apr. 2015) 92–105, https://doi.org/10.1016/j.neuron.2015.01.028.
[3] A.H. Marblestone, et al., Physical principles for scalable neural recording, Front. Comput. Neurosci. 7 (Oct. 2013), https://doi.org/10.3389/fncom.2013.00137.
[4] G.W. Gross, B.K. Rhoades, H.M.E. Azzazy, M.-C. Wu, The Use of Neuronal Networks on Multielectrode Arrays as Biosensors, 1995, https://doi.org/10.1016/0956-5663(95)96931-N.
[5] A. Stett, et al., Biological application of microelectrode arrays in drug discovery and basic research, Anal. Bioanal. Chem. 377 (3) (Oct. 2003) 486–495, https://doi.org/10.1007/s00216-003-2149-x.
[6] Y. Jimbo, H.P.C. Robinson, Propagation of Spontaneous Synchronized Activity in Cortical Slice Cultures Recorded by Planar Electrode Arrays, Jun. 2000, https://doi.org/10.1016/S0302-4598(99)00083-5.
[7] C.S. Cowan, et al., Cell types of the human retina and its organoids at single-cell resolution, Cell 182 (6) (Sep. 2020) 1623–1640, e34, https://doi.org/10.1016/j.cell.2020.08.013.
[8] J. Müller, et al., High-resolution CMOS MEA platform to study neurons at subcellular, cellular, and network levels, Lab Chip 15 (13) (Jul. 2015) 2767–2780, https://doi.org/10.1039/c5lc00133a.
[9] R. Thewes, et al., Neural tissue and brain interfacing CMOS devices — an introduction to state-of-the-art, current and future challenges, in: 2016 IEEE International Symposium on Circuits and Systems (ISCAS), IEEE, Aug. 2016, pp. 1826–1829, https://doi.org/10.1109/ISCAS.2016.7538925.
[10] G. Bertotti, et al., A CMOS-based sensor array for in-vitro neural tissue interfacing with 4225 recording sites and 1024 stimulation sites, in: 2014 IEEE Biomedical Circuits and Systems Conference (BioCAS), IEEE, Dec. 2014, pp. 304–307, https://doi.org/10.1109/BioCAS.2014.6981723.
[11] D.J. Bakkum, et al., Tracking axonal action potential propagation on a high-density microelectrode array across hundreds of sites, Nat. Commun. 4 (Jul. 2013), https://doi.org/10.1038/ncomms3181.
[12] A.P. Buccino, X. Yuan, V. Emmenegger, X. Xue, T. Gänswein, A. Hierlemann, An automated method for precise axon reconstruction from recordings of high-density micro-electrode arrays, J. Neural Eng. 19 (2) (Apr. 2022), https://doi.org/10.1088/1741-2552/ac59a2.
[13] I. Suzuki, et al., Large-area field potential imaging having single neuron resolution using 236 880 electrodes CMOS-MEA technology, Adv. Sci. 10 (20) (Apr. 2023) 2207732, https://doi.org/10.1002/advs.202207732.
[14] R. Zeitler, P. Fromherz, G. Zeck, Extracellular voltage noise probes the interface between retina and silicon chip, Appl. Phys. Lett. 99 (26) (Dec. 2011), https://doi.org/10.1063/1.3672224.
[15] M. Ell, M.T. Bui, S. Kigili, G. Zeck, S. Prado-López, Assessment of chemotherapeutic effects on cancer cells using adhesion noise spectroscopy, Front. Bioeng. Biotechnol. 12 (2024), https://doi.org/10.3389/fbioe.2024.1385730.
[16] A. Corna, P. Ramesh, F. Jetter, M.J. Lee, J.H. Macke, G. Zeck, Discrimination of simple objects decoded from the output of retinal ganglion cells upon sinusoidal electrical stimulation, J. Neural Eng. 18 (4) (Aug. 2021), https://doi.org/10.1088/1741-2552/ac0679.
[17] E.A. Vallicelli, et al., Neural spikes digital detector/sorting on FPGA, in: 2017 IEEE Biomedical Circuits and Systems Conference (BioCAS), IEEE, Mar. 2018, pp. 1–4, https://doi.org/10.1109/BIOCAS.2017.8325077.
[18] E.A. Vallicelli, et al., Real-time digital implementation of a principal component analysis algorithm for neurons spike detection, in: 2018 International Conference on IC Design & Technology (ICICDT), IEEE, Jul. 2018, pp. 33–36, https://doi.org/10.1109/ICICDT.2018.8399749.
[19] R. Zeitler, P. Fromherz, The thermal voltage fluctuations in the planar core-coat conductor of a neuron-semiconductor interface, Langmuir 29 (20) (May 2013) 6084–6090, https://doi.org/10.1021/la4002169.
[20] A. Corna, T. Herrmann, G. Zeck, Electrode-size dependent thresholds in subretinal neuroprosthetic stimulation, J. Neural Eng. 15 (4) (Jun. 2018), https://doi.org/10.1088/1741-2552/aac1c8.
[21] E.A. Vallicelli, et al., Neural spike digital detector on FPGA, Electronics (Switzerland) 7 (12) (Dec. 2018), https://doi.org/10.3390/electronics7120392.
[22] M. Tambaro, et al., A 10 MSample/Sec digital neural spike detection for a 1024 pixels multi transistor array sensor, in: 2019 26th IEEE International Conference on

Electronics, Circuits and Systems (ICECS), IEEE, Jan. 2020, pp. 711–714, https://doi.org/10.1109/ICECS46596.2019.8965141.
[23] M. Tambaro, et al., Real-time neural (RT-Neu) spikes imaging by a 9375 sample/(sec pixel) 32×32 pixels electrolyte-oxide-semiconductor biosensor, in: 2019 15th Conference on Ph.D Research in Microelectronics and Electronics (PRIME), IEEE, Aug. 2019, p. 312, https://doi.org/10.1109/PRIME.2019.8787817.
[24] A. Castillo Atoche, R. Carrasco Alvarez, O. Palma Marrufo, J. Vázquez Castillo, An efficient systolic array grid-based structure of the robust Bayesian regularization technique for real-time enhanced imaging in uncertain remote sensing environment, J. Real-Time Image Proc. 13 (Dec. 2017) 783–796, https://doi.org/10.1007/s11554-014-0441-y.
[25] V.V. Zunin, I.I. Romanova, Parameterized computing module generator based on a systolic array, in: 2022 IEEE International Conference on Industry 4.0, Artificial Intelligence, and Communications Technology (IAICT), IEEE, Sep. 2022, pp. 217–220, https://doi.org/10.1109/IAICT55358.2022.9887460.
[26] S. Ramadurgam, D.G. Perera, A systolic array architecture for SVM classifier for machine learning on embedded devices, in: 2023 IEEE International Symposium on Circuits and Systems (ISCAS), IEEE, Jul. 2023, pp. 1–5, https://doi.org/10.1109/ISCAS46773.2023.10182159.
[27] FIR Compiler v7.2 - LogiCORE IP Product Guide Vivado Design Suite (PG149), AMD Xilinx, 2024. Accessed: Jun. 17, 2024. [Online]. Available: https://www.xilinx.com/support/documents/ip_documentation/fir_compiler/v7_2/pg149-fir-compiler.pdf.
[28] Vivado Design Suite AXI Reference Guide (UG1037), AMD Xilinx, 2024. Accessed: Jun. 19, 2024. [Online]. Available: https://docs.amd.com/v/u/en-US/ug1037-vivado-axi-reference-guide.
[29] UltraFast Design Methodology Guide for FPGAs and SoCs (UG949), AMD Technical Information Portal, 2024. Accessed: Jun. 16, 2024. [Online]. Available: https://docs.amd.com/r/en-US/ug949-vivado-design-methodology.
[30] M. Ell, A. Büyükakyüz, G. Zeck, Digital filter on FPGA for neuronal spike detection recorded by a CMOS-based microelectrode array, in: Proceedings of the Austrian Workshop on Microelectronics, Austrochip, IEEE, Oct. 2024, https://doi.org/10.1109/Austrochip62761.2024.10716224.
[31] R.M. Haralick, L.G. Shapiro, Computer and Robot Vision 1, Addison-Wesley, 1992.
[32] N. Otsu, A threshold selection method from gray-level histograms, IEEE Trans. Syst. Man Cybern. 9 (1) (Jan. 1979) 62–66, https://doi.org/10.1109/TSMC.1979.4310076.
[33] A. Corna, A.E. Cojocaru, M.T. Bui, P. Werginz, G. Zeck, Avoidance of axonal stimulation with sinusoidal epiretinal stimulation, J. Neural Eng. 21 (2) (Apr. 2024), https://doi.org/10.1088/1741-2552/ad38de.
[34] F. Leva, A. Corna, P. Werginz, P. Palestri, G. Zeck, L. Selmi, Identification of axon bendings in neurons by multiphysics FEM simulations of high-density MEA extracellular recordings, in: Proceedings of IEEE Sensors, IEEE, Nov. 2023, pp. 1–4, https://doi.org/10.1109/SENSORS56945.2023.10325212.
[35] S. Preibisch, S. Saalfeld, P. Tomancak, Globally optimal stitching of tiled 3D microscopic image acquisitions, Bioinformatics 25 (11) (Apr. 2009) 1463–1465, https://doi.org/10.1093/bioinformatics/btp184.
[36] P.R.F. Rocha, et al., Electrochemical noise and impedance of Au electrode/electrolyte interfaces enabling extracellular detection of glioma cell populations, Sci. Rep. 6 (Oct. 2016), https://doi.org/10.1038/srep34843.
[37] M. Ell, R. Zeitler, R. Thewes, G. Zeck, Label-free identification of nonelectrogenic cancer cells using adhesion noise, in: 2023 IEEE BioSensors Conference, BioSensors 2023 - Proceedings, IEEE, London, Oct. 2023, pp. 1–4, https://doi.org/10.1109/BioSensors58001.2023.10280952.
[38] M. Voelker, P. Fromherz, Nyquist noise of cell adhesion detected in a neuron-silicon transistor, Phys. Rev. Lett. 96 (22) (Jun. 2006) 228102, https://doi.org/10.1103/PhysRevLett.96.228102.
[39] M.J. Berry, D.K. Warland, M. Meister, The structure and precision of retinal spike trains, Proc. Natl. Acad. Sci. USA 94 (10) (May 1997) 5411–5416, https://doi.org/10.1073/pnas.94.10.5411.
[40] E.R. Kandel, J.H. Schwartz, T.M. Jessell, S.A. Siegelbaum, A.J. Hudspeth, S. Mack, Principles of Neural Science, The McGraw-Hill Companies, Inc., 2013.
[41] Y. Fukuda, M. Watanabe, K. Wakakuwa, H. Sawai, K. Morigiwa, Intraretinal axons of ganglion cells in the Japanese monkey (*Macaca fuscata*): conduction velocity and diameter distribution, Neurosci. Res. 6 (1) (Oct. 1988) 53–71, https://doi.org/10.1016/0168-0102(88)90006-5.
[42] B.L.R. Rabiner, J.F. Kaiser, O. Herrmann, M.T. Dolan, Some comparisons between FIR and MR digital filters, Bell Syst. Tech. J. 53 (2) (Feb. 1974) 305–331, https://doi.org/10.1002/j.1538-7305.1974.tb02745.x.
[43] M. Najim, Digital Filters Design for Signal and Image Processing, Wiley & Sons Ltd, 2006.
[44] K.J. Bender, L.O. Trussell, The physiology of the axon initial segment, Annu. Rev. Neurosci. 35 (Jul. 2012) 249–265, https://doi.org/10.1146/annurev-neuro-062111-150339.
[45] C. Donner, et al., Ensemble learning and ground-truth validation of synaptic connectivity inferred from spike trains, PLoS Comput. Biol. 20 (4) (Apr. 2024), https://doi.org/10.1371/journal.pcbi.1011964.
[46] E. Lazarov, et al., An axon initial segment is required for temporal precision in action potential encoding by neuronal populations, Sci. Adv. 4 (11) (Nov. 2018), https://doi.org/10.1126/sciadv.aau8621.
[47] V. Iyer, D.A. Issadore, F. Aflatouni, The Next Generation of Hybrid Microfluidic/Integrated Circuit Chips: Recent and Upcoming Advances in High-Speed, High-Throughput, and Multifunctional Lab-on-IC Systems, Royal Society of Chemistry, Apr. 2023, https://doi.org/10.1039/d2lc01163h.
[48] C. Laborde, et al., Real-time imaging of microparticles and living cells with CMOS nanocapacitor arrays, Nat. Nanotechnol. 10 (9) (Sep. 2015) 791–795, https://doi.org/10.1038/nnano.2015.163.
[49] F. Widdershoven, et al., A CMOS pixelated nanocapacitor biosensor platform for high-frequency impedance spectroscopy and imaging, IEEE Trans. Biomed. Circuits Syst. 12 (6) (Dec. 2018) 1369–1382, https://doi.org/10.1109/TBCAS.2018.2861558.